Advances in Geo-Energy Research

Vol. 16, No. 3, p. 199-210, 2025

Original article

Effect of confinement on the vapor-liquid-liquid three-phase equilibrium during CO_2 utilization and sequestration in shale reservoirs

Zhuo Chen[1], Ruixue Li[2,3]*, Yifei Du[2], Shunting Ma[2], Xin Zhang[4], Jialin Shi[5]

[1]*Department of Chemical and Materials Engineering, University of Alberta, Edmonton T6G 2V4, Canada*

[2]*College of Energy, Chengdu University of Technology, Chengdu 610059, P. R. China*

[3]*State Key Laboratory of Oil and Gas Reservoir Geology and Exploitation (Chengdu University of Technology), Chengdu 610059, P. R. China*

[4]*School of Mining and Petroleum Engineering, University of Alberta, Edmonton T6G 1H9, Canada*

[5]*State Key Laboratory of Chemical Engineering, School of Chemistry and Molecular Engineering, East China University of Science and Technology, Shanghai 200237, P. R. China*

Keywords:
CO_2 utilization
carbon sequestration
three-phase equilibrium
shale reservoir
confinement effect
phase behavior

Cited as:
Chen, Z., Li, R., Du, Y., Ma, S., Zhang, X., Shi, J. Effect of confinement on the vapor-liquid-liquid three-phase equilibrium during CO_2 utilization and sequestration in shale reservoirs. Advances in Geo-Energy Research, 2025, 16(3): 199-210.
https://doi.org/10.46690/ager.2025.06.02

Abstract:
With the rising global energy demand, shale gas and oil emerge as pivotal resources. Recent innovations utilizing CO_2 as an injectant can effectively enhance shale oil and gas recovery and facilitate CO_2 storage within shale reservoirs. However, low-temperature CO_2 injection may result in the coexistence of three hydrocarbon phases, while the abundant nanopores in shale formations also notably influence the phase behavior of reservoir fluids. To optimize shale oil recovery and CO_2 sequestration in shale formations, it is a prerequisite for precisely capturing the effect of confinement on the phase behavior of reservoir fluids within nanopores during CO_2 injection. In this work, we introduce a novel three-phase vapor-liquid-liquid equilibrium calculation algorithm, which is designed to handle the unique phase behavior challenges presented by CO_2 utilization and storage in shale reservoirs. To improve the robustness and efficiency, the proposed algorithm integrates a trust region-based stability test with a hybrid flash calculation algorithm that combines the Newton-Raphson and trust-region methods. Our thermodynamic model incorporates the capillarity effect and shifts in the critical points due to molecule-wall interactions, which are essential for accurate phase behavior simulation under confinement. Initial validations against experimental bulk phase data show promising results, and further investigations indicate that confinement alters three-phase vapor-liquid-liquid equilibria by suppressing two-phase and three-phase regions and shifting boundaries in the phase diagrams. The proposed algorithm not only advances our understanding of multiphase equilibrium in nanoporous media but also enhances the practicality of CO_2 sequestration and improved oil recovery strategies in shale formations.

1. Introduction

The combustion of fossil fuels releases anthropogenic CO_2, contributing to climate change and atmospheric warming (Chen et al., 2022). The Paris Agreement recognizes that these phenomena threaten human societies and various natural ecosystems (Andersen et al., 2020). Meanwhile, the global demand for affordable, reliable energy continues to rise

Yandy Scientific Press

*Corresponding author.
E-mail address: zhuo8@ualberta.ca (Z. Chen); liruixue19@cdut.edu.cn (R. Li); duyifei@stu.cdut.edu.cn (Y. Du); ting80693691@163.com (S. Ma); xz20@ualberta.ca (X. Zhang); jialinshi@ecust.edu.cn (J. Shi).

Received February 6, 2025; revised March 1, 2025; accepted March 28, 2025; available online April 3, 2025.

(Andersen et al., 2020). Shale oil, expected to significantly boost crude production worldwide, has become a critical part of the energy industry. With global reserves estimated at 67,840 × 108 barrels, technological advances in hydraulic fracturing and horizontal drilling continue to enhance shale oil extraction (Song et al., 2019). However, the recovery rates from shale formations remain suboptimal. Recent innovations include the use of CO_2 as an injectant to enhance oil recovery rates and facilitate CO_2 storage in depleted shale reservoirs, which offers a dual benefit of enhanced oil recovery and CO_2 sequestration (Andersen et al., 2020; Chen et al., 2022). This approach has garnered increasing interest mostly due to its potential to efficiently manage CO_2 emissions, although it complicates the thermodynamic properties and interphase mass transfers of formation fluids in shale reservoirs. In order to enhance the efficiency of shale oil and gas production and CO_2 storage in shale reservoirs, it is essential to develop an accurate and robust thermodynamic model to simulate the phase behavior in such reservoirs.

Fluid phase behavior in nanopores differs markedly from that in conventional bulk environments (Liu and Zhang, 2019). Shale formations, abundant with nanopores, exhibit varied pore sizes that influence phase behavior significantly (Yang et al., 2019). For example, the Middle Bakken shale features pore sizes between 30-50 nm, the Niobrara Formation has 4-11 nm, and the Fayetteville shale ranges from 5-100 nm (Bai et al., 2013). These meso- and nanopores introduce notable deviations in the fluid properties and phase behavior compared to conventional reservoirs, impacting shale reservoir production with increased uncertainty. Two primary phenomena illustrate the effect of confinement on reservoir fluids (Liu and Zhang, 2019). The first involves capillary pressure, which is often overlooked in conventional phase equilibrium calculations where gas and oil pressures are assumed equal (Liu and Zhang, 2019). However, in shale reservoirs, the effect of confinement elevates the capillary pressure to a level that cannot be ignored. Methods to evaluate capillary pressure include the Young-Laplace equation (Young, 1805), the Leverett J-function curve (Leverett, 1941), and flexible models, with the Young-Laplace equation being the most prevalent due to its simplicity and relatively accurate results. Despite its usefulness, the Young-Laplace equation falls short at the critical point where capillary pressure is negligible, failing to account for shifts in the fluid critical point caused by strong molecule-wall interactions (Liu and Zhang, 2019). To address this issue, the consideration of capillary pressure is often augmented with critical shift equations, ensuring a more comprehensive understanding of phase behavior in confined spaces (Sun and Li, 2021).

During CO_2 utilization and storage in shale reservoirs, the injection of CO_2 into oil reservoirs at low temperatures can result in the formation of up to three distinct hydrocarbon phases: Vapor Phase (V), Oil-rich Liquid Phase (L_1), and CO_2-rich Liquid Phase (L_2) (Li et al., 2013; Chen et al., 2023, 2024). The emergence of the secondary liquid phase significantly influences oil recovery efficiency by modifying the relative permeability of different phases (Li et al., 2013). Therefore, it is essential to develop a pragmatic algorithm that accurately captures the three-phase vapor-liquid-liquid (VL_1L_2) equilibrium. Michelsen introduced the first systematic multiphase flash approach to perform the three-phase VL_1L_2 equilibrium calculations (Michelsen, 1982b). Traditionally, Newton's method, guided by the initial estimates from the successive substitution method, is employed for phase equilibrium calculations. Despite the rapid convergence of this method, issues often arise near-critical regions or during stability tests (Lu et al., 2021). To address these challenges, Petitfrere and Nichita, 2014 recommended a Trust Region (TR) method, particularly when Newton's method is insufficient. This inspired Pan et al. (2019) to develop a TR-based multiphase equilibrium calculation algorithm. The algorithm begins with a two-phase flash following a single-phase stability test, then tests the stability of each phase resulting from the flash. If instability is detected, a three-phase flash is initiated. The algorithm incorporates various initialization methods to handle failures in flash calculations effectively. Tested on tens of millions of data points without error, it proved highly effective for modeling CO_2-crude oil phase behavior in low-temperature reservoirs. This method was later enhanced by Xu et al. (2023) through a hybrid approach combining Newton-Raphson (NR) and TR methods, resulting in increased computational efficiency and enhanced robustness. However, the existing algorithms for VL_1L_2 three-phase equilibrium calculations do not account for the effects of confinement, rendering them unsuitable for simulating phase behavior in the nanopores of shale reservoirs during CO_2 injection.

This paper introduces a novel three-phase VL_1L_2 equilibrium calculation algorithm tailored for simulating the phase behavior of CO_2 utilization and sequestration processes in shale reservoirs. The algorithm incorporates the effects of capillary pressure and critical point shift to accurately simulate phase behavior in confined nanopores. To enhance robustness, the algorithm integrates the initialization method and TR-based stability test approach originally proposed by Pan et al. (2019). Furthermore, it employs the hybrid flash calculation algorithm developed by Xu et al. (2023), which combines NR and TR methods while using both equilibrium ratios and phase fractions as iterative variables to improve computational efficiency and algorithm stability. The proposed algorithm was first validated by comparing calculation results with experimental data under bulk conditions. Subsequently, the impacts of confinement on the pressure-temperature (PT) and pressure-composition (Px) phase diagrams were explored using the validated algorithm. Additionally, the influence of varying pore radii on these phase behaviors was investigated.

2. Methodology

2.1 Thermodynamic model

The equal-fugacity constraint is required to be satisfied during the three-phase VL_1L_2 equilibrium calculations:

$$f_i^V = f_i^{(L_1)} = f_i^{(L_2)} \tag{1}$$

where f represents the fugacity, bar; the subscripts i represents the i^{th} component; the superscript V, L_1, and L_2 stand for vapor phase, oil-rich liquid phase, and CO_2-rich liquid phase,

respectively. In this research, the Peng-Robinson Equation of State (PR-EOS) (Peng and Robinson, 1976) is employed to calculate the fugacity of each phase, offering an optimal balance between computational efficiency and accuracy for the hydrocarbon systems under investigation. While cubic EOS have known limitations in highly confined systems, the pore sizes in our study allow for a reasonable application of PR-EOS with appropriate modifications.

To precisely capture the phase behavior of fluids in nanopores, this study incorporates both the shift in critical properties and the capillary effect into the phase equilibrium calculation model. Zhang et al. (2018) established the relationship between the shifts in critical pressures and temperatures of confined fluids and the radius of nanopores as follows:

$$\Delta T_c^* = \frac{T_{cb} - T_{cp}}{T_{cb}} = \frac{0.7197\sigma_{LJ}}{r} - \frac{0.0758\sigma_{LJ}^2}{r^2} \tag{2}$$

$$\Delta P_c^* = P_{cb} - P_{cp}P_cb = \frac{0.7197\sigma_{LJ}}{r} - \frac{0.0758\sigma_{LJ}^2}{r^2} \tag{3}$$

where T_{cb} and T_{cp} represent the critical temperature of the bulk phase fluid and confined fluid, respectively, K; P_{cb} and P_{cp} stand for the critical pressure of the bulk phase fluid and confined fluid, respectively, bar; r denotes the radius of nanopores, nm; σ_{LJ} represents the Lennard-Jones fluid sizing parameter, nm (Hirschfelder et al., 1964):

$$\sigma_{LJ} = 0.244\sqrt[3]{\frac{T_{cb}}{P_{cb}}} \tag{4}$$

The pressure equilibrium between three phases in nanopores under capillary effects is shown in Fig. 1 and can be represented by:

$$P_V = P_{L1} + P_{C1} + P_{C2} = P_{L2} + P_{C2} \tag{5}$$

where P_V, P_{L1}, and P_{L2} are the equilibrium pressures of vapor phase, oil-rich liquid phase, and CO_2-rich liquid phase, respectively, bar; P_{C1} and P_{C2} denote the capillary pressure between the oil-rich liquid phase and CO_2-rich liquid phase and between the vapor phase and CO_2-rich liquid phase, respectively, bar.

The capillary pressure is calculated by (Young, 1805):

$$P_c = \frac{2\sigma\cos\theta}{r} \tag{6}$$

where σ represents interfacial tension (IFT), mN/m; θ is the contact angle. In this study, θ is assumed to be zero to examine the general trend of capillary pressure influence on the system. To account for the influence of fluid composition on capillary pressure, the interfacial tension can be obtained as follows (Weinaug and Katz, 1943):

$$\sigma = \left[\sum_{i=1}^{nc} P_{chi}\left(\rho_w x_i - \rho_{nw} y_i\right)\right]^4 \tag{7}$$

where nc represents the number of components; ρ_w and ρ_{nw} are the density of the wetting phase and the non-wetting phase, respectively, g/cm^3; x_i and y_i stand for the mole fractions of the wetting phase and the non-wetting phase, respectively; P_{chi} represents the Parachor constant of the i^{th} component (Firoozabadi et al., 1988):

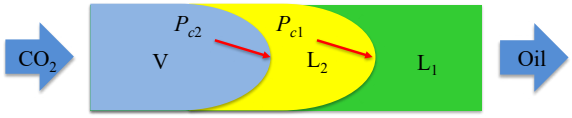

Fig. 1. Schematic showing the pressure equilibrium among the three phases in nanopores.

$$P_{chi} = -11.4 + 3.23M_i - 0.0022M_i^2 \tag{8}$$

where M_i is the molecular weight of the i^{th} component, g/mol. However, when the pore size is below 10 nm, the adsorption effects can play a predominant role, and solely considering the capillary forces and critical point shift may lead to inaccuracies in phase equilibrium calculations. Therefore, this study primarily focuses on analyzing the impact of pore size variations on phase equilibrium for pore sizes larger than 10 nm.

2.2 Phase stability test

The phase stability test determines whether a mixture will remain as a single phase or separate into multiple phases at specified temperature and pressure conditions. In mathematical terms, it evaluates whether a hypothetical perturbation in composition would reduce the system's Gibbs free energy, indicating phase instability. The mixture is stable when all tangent plane distance values are non-negative. The tangent plane distance function of the confined fluid is given below (Sherafati and Jessen, 2017):

$$g(\boldsymbol{w}) = \sum_{i=1}^{nc} w_i\left(\ln\phi_{iw} - \ln w_i + P_w - \ln\phi_{iz} - \ln z_i - P_z\right) \tag{9}$$

where w_i represents the composition of the trial phase, and z_i represents the composition of the tested phases, respectively. ϕ is the fugacity coefficient. P signifies the phase pressure. Subscripts w and z indicate the trial and tested phases. When solving the tangent plane distance function, the compressibility factors of the tested phase and trial phase must be compared in each iteration to determine P_w and P_z. When the tested phase exhibits a lower compressibility factor, P_z equals the specified pressure, and $P_w = P_z + P_c$. Otherwise, P_w and P_z values must be interchanged. Michelsen (1982a) provides the detailed procedures for the stability test. To ensure robust and reliable results, the stability test incorporates multiple initial equilibrium ratio estimates: K_i^{Wilson}, $1/K_i^{Wilson}$, $\sqrt[2]{K_i^{Wilson}}$, $\sqrt[3]{1/K_i^{Wilson}}$, $K_i^{CO_2}$, K_i^{nc} (Michelsen, 1982a; Li and Firoozabadi, 2012; Pan et al., 2019), where:

$$K_i^{CO_2} = \begin{cases} \dfrac{0.9}{z_{CO_2}}, & i = CO_2 \\ \dfrac{0.1}{z_i(nc-1)}, & i \neq CO_2 \end{cases} \qquad i = 1,2,\cdots,nc \tag{10}$$

$$K_i^{nc} = \begin{cases} \dfrac{0.9}{z_{nc}}, & i = nc \\ \dfrac{0.1}{z_i(nc-1)}, & i = 1,2,\cdots,nc-1 \end{cases}$$

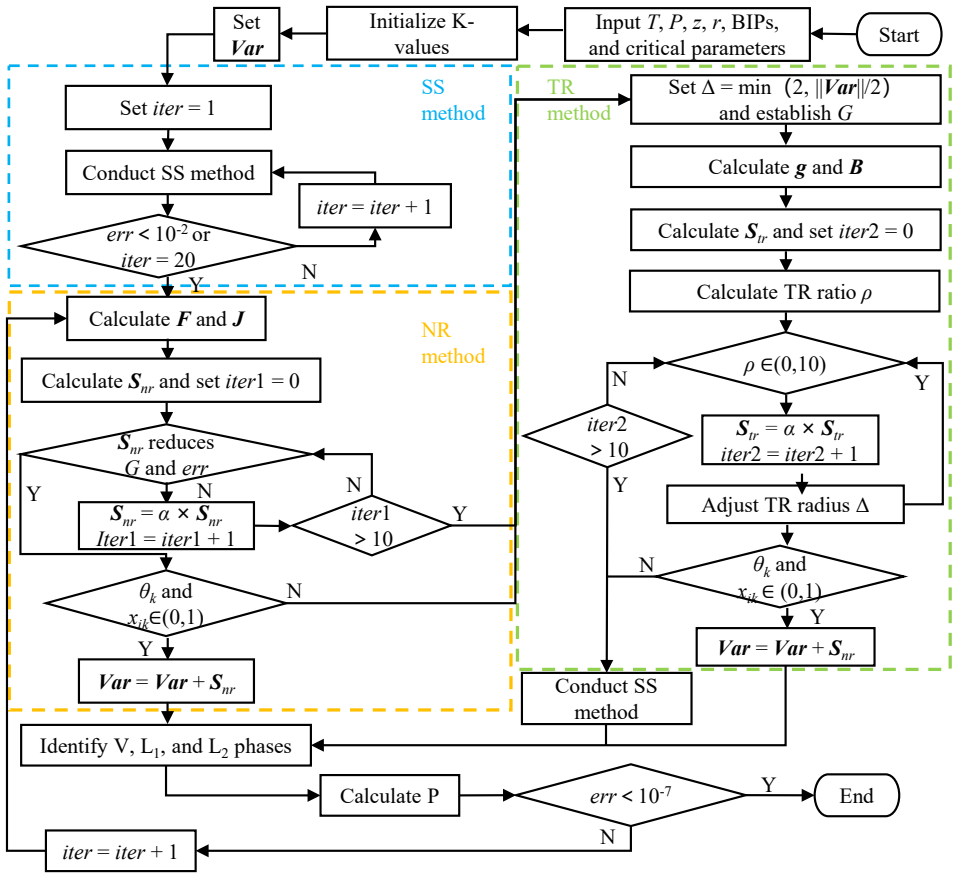

Fig. 2. Flowchart outlining the flash calculation algorithm for confined fluids.

K_i^{Wilson} represents the equilibrium ratio of the i^{th} component calculated by Wilson equation (Wilson, 1969):

$$K_i^{Wilson} = \frac{P_{ci}\exp\left[5.37\,(1+\omega_i)\left(1-\frac{T_{ci}}{T}\right)\right]}{P} \tag{11}$$

where T_{ci} denotes critical temperature of component i. P_{ci} is the critical pressure. ω represents the acentric factor. The algorithm for the TR-based stability test closely follows the one proposed by Pan et al. (2019).

2.3 Flash calculation algorithm based on hybrid NR and TR method

The previous research indicates that relying solely on the SS (successive substitution) method (Robinson et al., 1985) and the NR method (Robinson et al., 1985; Petitfrere and Nichita, 2016) for multi-phase flash calculations, especially in the presence of three-phase VL_1L_2 phase equilibrium, may fail to achieve convergence (Pan et al., 2019). To enhance the robustness of the flash calculation algorithm, it is necessary to introduce the TR method in addition to the SS and NR methods (Petitfrere and Nichita, 2014; Pan et al., 2019; Xu et al., 2023). Following the approach proposed by Xu et al. (2023), the algorithm initially executes the conventional SS method until the error falls below 10^{-2}. Subsequently, the NR method is applied. If the NR method proves inadequate, the TR method is then utilized. If even the TR method is unsatisfactory, the algorithm ultimately reverts to the SS method. To ensure model stability, the developed framework employs multiple convergence algorithms, which to some extent sacrifice computational efficiency. Nevertheless, the overall approach prioritizes stability while optimizing computational performance to the greatest extent possible. To effectively apply the flash calculation algorithm to confined fluids, the compressibility factor of each phase must be computed after the components of each phase are determined in each iteration. This facilitates the differentiation between vapor phase, solvent-rich liquid phase, and oil-rich liquid phase, enabling the subsequent calculation of the pressure of each phase using Eq. (5). Fig. 2 presents the flowchart outlining the flash calculation algorithm for confined fluids, and the detailed steps are enumerated as follows:

1) Set the independent variables required in the flash calculation as a vector named $\boldsymbol{Var}$. $\boldsymbol{Var}$ is expressed as follows (Petitfrere and Nichita, 2016):

$$\boldsymbol{Var} = \left[\ln \boldsymbol{K}_{\boldsymbol{1}}^T, \cdots, \ln \boldsymbol{K}_{np-1}^T, \boldsymbol{\theta}^T\right]^T \tag{12}$$

where

$$\boldsymbol{K}_k = \left[\ln K_{1,k}, \cdots, K_{nc,k}\right]^T,\ k = 1, \cdots, np-1 \tag{13}$$

$$\boldsymbol{\theta} = \left[\theta_1, \cdots, \theta_{np-1}\right]^T \tag{14}$$

where np denotes the number of phases; K represents the equilibrium ratio; θ stands for the phase fraction.

2) Initialize the equilibrium ratios based on the stability test results. Then, perform the flash calculations using the conventional SS method (Robinson et al., 1985) iteratively until the error falls below 10^{-2} or the iteration number exceeds 20. For confined fluids, the error is calculated by:

$$err = \sqrt{\sum_{i=1}^{nc}\sum_{k=1}^{np-1}(f_{ik}-f_{i,np})^2} + \sqrt{\sum_{k=1}^{np-1}\left(P_{ck}^{n-1}-P_{ck}^{n}\right)^2} \tag{15}$$

where P_c represents the capillary pressure, n denotes the number of iterations, and f stands for fugacity. Noted that for a three-phase VL_1L_2 flash calculation involving confined fluids, prior to calculating the fugacity at each iteration, the compressibility factor of each phase must be computed first in order to identify whether the phase is vapor phase, solvent-rich liquid phase, or oil-rich liquid phase. Subsequently, the capillary pressure between phases and the equilibrium pressure of each phase are calculated. These equilibrium pressures are then input into the PR-EOS (Peng and Robinson, 1976) to determine the fugacity of each component in each phase.

3) The results obtained from the SS method are used to calculate the objective function $\boldsymbol{F}$ and its Jacobian matrix $\boldsymbol{J}$ of the NR method. The objective function $\boldsymbol{F}$ is expressed as in Eq. (18) (Haugen et al., 2011; Petitfrere and Nichita, 2016), and the detailed expression of the Jacobian matrix $\boldsymbol{J}$ can be referenced from Xu et al. (2023):

$$\boldsymbol{F} = \left[\boldsymbol{g_1}^T, \cdots, \boldsymbol{g}_{np-1}^T, R_1, ..., R_{np-1}\right]^T \tag{16}$$

where

$$\boldsymbol{g_k} = [g_{ik}, \cdots, g_{nc,k}]^T,\ k = 1, \cdots, np-1 \tag{17}$$

$$g_{ik} = \frac{\partial G}{\partial n_{ik}} = \ln K_{ik} + \ln \varphi_{ik} - \ln \varphi_{i,np} \tag{18}$$

$$R_k = \sum_{i=1}^{nc} \frac{z_i(K_{ik}-1)}{1+\sum_{l=1}^{np-1}\theta_l(K_{il}-1)} \tag{19}$$

where G represents the dimensionless Gibbs free energy, R stands for the Rachford and Rice equation (Rachford Jr and Rich, 1952), and ϕ is the fugacity coefficient.

4) Determine the updated step size of NR method $\boldsymbol{S}_{nr}$ based on $\boldsymbol{JS}_{nr} = -F$ and update Var by $\boldsymbol{Var}^{n+1} = \boldsymbol{Var}^n + \boldsymbol{S}_{nr}$. Check if the updated $\boldsymbol{Var}$ results in a decrease in the Gibbs free energy and the error. If so, proceed to Step 5. Otherwise, reduce the step size by $\boldsymbol{S}_{nr} = \alpha \times \boldsymbol{S}_{nr}$, where α is a constant between 0 and 1. In this study, α is set to 0.5. If after 10 updates of $\boldsymbol{S}_{nr}$, the condition is still not met, proceed to Step 6.

5) Determine the phase fractions and compositions on the basis of the updated $\boldsymbol{Var}$. If they all fall within the range of 0 to 1, compute the error. If not, proceed to Step 6. If the error is less than 10^{-7}, terminate the process. Otherwise, return to Step 3.

6) Perform flash calculations using the TR method (Petitfrere and Nichita, 2014; Pan et al., 2019). First, set the initial TR radius as $\Delta = \min(2, ||\boldsymbol{Var}||/2)$ and establish the objective function G for the TR method according to Xu et al. (2023) as follows:

$$G = \sum_{k=1}^{np}\sum_{i=1}^{nc} n_{ik} \ln f_{ik}(x_k) \tag{20}$$

In this equation, both the mole number n_{ik} and mole fraction x_{ik} are functions of $\boldsymbol{Var}$. Therefore, G is a function of $\boldsymbol{Var}$.

7) Compute the gradient vector $\boldsymbol{g}$ and the Hessian matrix $\boldsymbol{B}$ of the objective function G. The detailed equation of the gradient vector $\boldsymbol{g}$ can be referenced from Xu et al. (2023), while the Hessian matrix $\boldsymbol{B}$ can be calculated using the Broyden-Fletcher-Goldfarb-Shanno method (Nocedal and Wright, 2006). The Hessian matrix $\boldsymbol{B}$ is updated as follows (Nocedal and Wright, 2006):

$$\boldsymbol{B}^{n+1} = \boldsymbol{B}^n + \frac{\boldsymbol{y}^n(\boldsymbol{y}^n)^T}{(\boldsymbol{y}^n)^T\boldsymbol{p}^n} - \frac{\boldsymbol{B}^n\boldsymbol{p}^n(\boldsymbol{p}^n)^T\boldsymbol{B}^n}{(\boldsymbol{p}^n)^T\boldsymbol{B}^n\boldsymbol{p}^n} \tag{21}$$

where $\boldsymbol{B}^l = \boldsymbol{I}$ and

$$\boldsymbol{y}^n = \boldsymbol{g}^n - \boldsymbol{g}^{n-1},\ n > 1 \tag{22}$$

$$\boldsymbol{p}^n = \boldsymbol{Var}^n - \boldsymbol{Var}^{n-1},\ n > 1 \tag{23}$$

8) Calculate the step size of TR method $\boldsymbol{S}_{tr}$ on the basis of $(\boldsymbol{H}+\lambda\boldsymbol{I})\boldsymbol{S}_{tr} = -\boldsymbol{g}$. Here, λ is a scalar and no smaller than 0 (Pan et al., 2019). The detailed method of calculating $\boldsymbol{S}_{tr}$ is proposed by Conn et al. (2000).

9) Calculate the TR ratio ρ by the following equation (Nocedal and Wright, 2006; Pan et al., 2019):

$$\rho^n = \frac{G(\boldsymbol{Var}^n) - G(\boldsymbol{Var}^n + \boldsymbol{S}_{tr}^n)}{m^n(\boldsymbol{Var}^n) - m^n(\boldsymbol{Var}^n + \boldsymbol{S}_{tr}^n)} \tag{24}$$

where the model function m in terms of the TR step $\boldsymbol{S}_{tr}$ is calculated by Nocedal and Wright (2006).

$$m^n(\boldsymbol{Var}^n) = G^n + (\boldsymbol{g}^n)^T\boldsymbol{S}_{tr}^n + 0.5(\boldsymbol{S}_{tr}^n)^T\boldsymbol{B}^n\boldsymbol{S}_{tr}^n \tag{25}$$

If ρ falls within the range of (0, 10), proceed to step 10. Otherwise, reduce the step size by $\boldsymbol{S}_{tr} = \alpha \times \boldsymbol{S}_{tr}$, where α is a constant between 0 and 1. In this study, α set to 0.5. If the condition is still not met after 10 updates of $\boldsymbol{S}_{tr}$, proceed to Step 12.

10) Adjust the TR radius as follows: If the ratio $\rho < 0.25$, reduce the current radius Δ by multiplying it by 0.25. If ρ is greater than 0.75, increase the current radius Δ by multiplying it by 3.5. In all other cases, keep Δ unchanged (Xu et al., 2023).

11) Determine the phase and mole fractions using the updated $\boldsymbol{Var}$. Validate if they are all within (0, 1); if not, proceed to Step 12. Otherwise, calculate the error, if $err < 10^{-7}$, end the process. Otherwise, repeat from Step 3.

12) Update $\boldsymbol{Var}$ using the SS method, calculate the error, and if $err < 10^{-7}$, terminate the process. Otherwise, return to Step 3.

The three-phase VL_1L_2 phase equilibrium calculation algorithm employs a traditional workflow (Michelsen, 1982a, 1982b). This process begins with conducting a stability test on the given mixture under a specified condition. If the feed

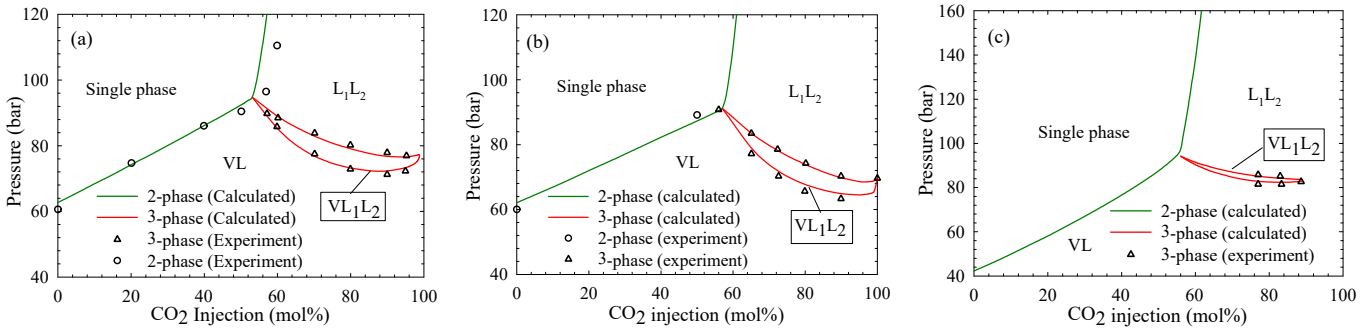

Fig. 3. Calculated *Px* phase diagrams versus experimental data: (a) Oil G at 307.59 K, (b) NWE oil at 301.48 K and (c) BSB oil at 313.71 K.

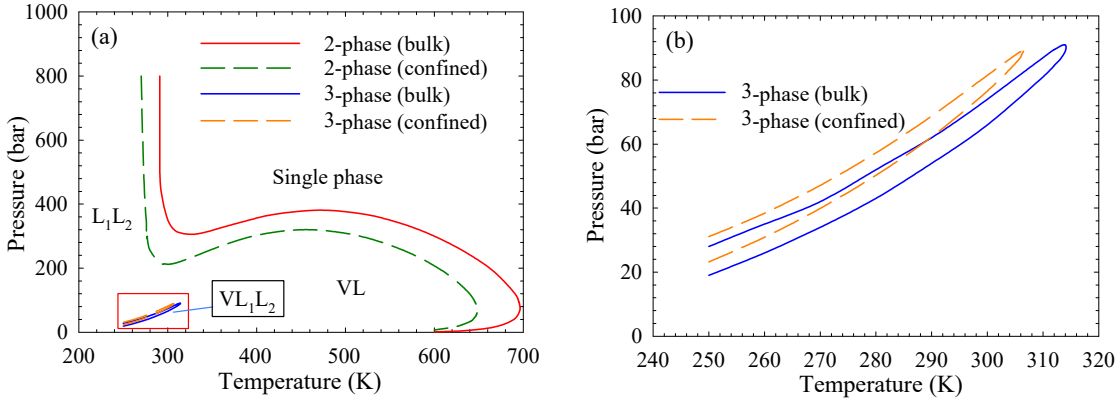

Fig. 4. Comparison between the *PT* phase diagrams of Oil G mixed with 70 mol% CO_2 at bulk and confined nanopores (10 nm): (a) Complete *PT* phase diagrams and (b) enlarged view of the VL_1L_2 three-phase region.

is found to be unstable, a two-phase flash calculation is conducted, and a stability test on the resulting flash calculation results is performed. If the two-phase system remains unstable, a three-phase flash calculation is subsequently undertaken. To bolster the robustness of this workflow, the improvement scheme proposed by Pan et al. (2019) has been integrated. The key enhancement therein is that if the first three-phase equilibrium calculation fails and there are additional trial phases available from the one-phase stability test, the aforementioned workflow will be repeated.

3. Results and discussion

3.1 Algorithm validation

Three oil samples from West Texas (Khan et al., 1992), known to form VL_1L_2 three-phase regions with gas injection, were selected for three-phase VL_1L_2 equilibrium calculations. The detailed characterization results of these oil samples are shown in Table 1. These tables also provide the binary interaction parameters (BIPs) between CO_2 and hydrocarbon components, which are determined by fitting experimental data for the phase boundaries under bulk conditions.

Fig. 3 illustrates the comparison between the calculated *Px* phase diagrams of the three oil samples by the newly proposed algorithm and the experimental data reported by Khan et al. (1992). The *Px* phase diagrams are constructed by calculating the phase behavior by incrementally varying the pressure at 0.1 bar intervals and the CO_2 mole fraction at 0.1% intervals. When a change in the number of phases occurred between two adjacent points in the pressure-CO_2 mole fraction grid, the phase boundary was defined as the average of the neighboring values. The figure demonstrates that the predictions of our algorithm closely match the experimental measurements for the phase transition boundaries, demonstrating its reliability for modeling the reservoir fluid phase behavior during low-temperature CO_2 injection.

3.2 Effect of confinement on phase diagrams

3.2.1 PT phase diagram

The effect of confinement on the *PT* phase diagrams was studied by using Oil G mixed with 70 mol% CO_2. Similar to the generation of the *Px* phase diagram, the *PT* phase diagrams were constructed by systematically evaluating the phase behavior of the fluid across a range of temperature and pressure conditions in increments of 0.1 bar and 0.1 K. When a phase transition occurred between two adjacent temperature-pressure points, the phase boundary was determined by calculating the midpoint between these neighboring conditions. Fig. 4(a) compares the *PT* phase diagrams of bulk Oil G with

Table 1. Characterization results of Oil G, NWE oil and BSB oil.

Sample	Component	T_c (K)	P_c (bar)	ω	MW (g/mol)	BIPs with CO_2	Composition (mol%)
Oil G	CO_2	304.200	73.76	0.225	44.010	0	1.690
	C_1	174.444	46.00	0.008	16.043	0.085	17.520
	C_{2-3}	347.263	44.69	0.133	37.909	0.085	22.440
	C_{4-6}	459.740	34.18	0.236	68.672	0.085	16.730
	C_{7-14}	595.135	21.87	0.598	135.093	0.104	24.220
	C_{15-25}	729.981	16.04	0.912	261.103	0.104	12.160
	C_{26+}	910.183	15.21	1.244	479.698	0.104	5.240
NWE oil	CO_2	304.200	73.77	0.225	44.010	0	0.770
	C_1	190.600	46.00	0.008	16.040	0.100	20.250
	C_{2-3}	343.640	45.05	0.130	38.400	0.100	11.800
	C_{4-6}	466.410	33.51	0.244	72.820	0.100	14.840
	C_{7-14}	603.070	24.24	0.600	135.820	0.070	28.630
	C_{15-24}	733.790	18.03	0.903	257.750	0.070	14.900
	C_{25+}	923.200	17.26	1.229	479.950	0.070	8.810
BSB oil	CO_2	304.200	73.77	0.225	44.010	0	3.370
	C_1	160.000	46.00	0.008	16.040	0.080	8.610
	C_{2-3}	344.205	44.99	0.131	37.200	0.080	15.030
	C_{4-6}	463.222	34.00	0.240	69.500	0.080	16.710
	C_{7-15}	605.752	21.75	0.618	140.960	0.100	33.040
	C_{16-27}	751.019	16.54	0.957	280.990	0.100	16.110
	C_{28+}	942.479	16.42	1.268	519.620	0.100	7.130

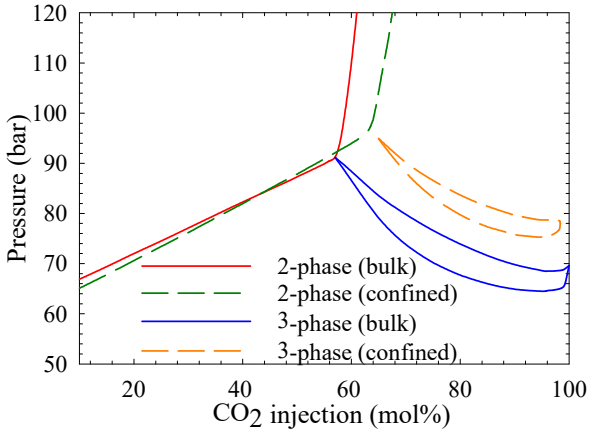

Fig. 5. Comparison between the *Px* phase diagrams in bulk phase and in confined nanopores (10 nm) of NWE Oil at 301.48 K.

those in 10 nm nanopores. Fig. 4(b) offers an enlarged view of the VL_1L_2 three-phase region, highlighting the impact of confinement on the VL_1L_2 three-phase boundary more clearly. As seen in Fig. 4, the single-phase/two-phase boundary shifts to the lower left due to the confinement effect, causing the two-phase region to shrink. This phenomenon indicates that CO_2 and reservoir fluids are more likely to become miscible within nanopores compared to the bulk phase. On the other hand, although the VL_1L_2 three-phase region also diminishes in size within the confined nanopores in the *PT* phase diagram, unlike the phase boundary between the single-phase region and the two-phase region, the VL_1L_2 three-phase region shifts to the upper left side in the *PT* phase diagram, indicating that in confined spaces, this three-phase region appears at higher pressures compared to that of bulk fluids.

3.2.2 *Px* phase diagram

Oil NWE was selected to demonstrate the effect of confinement on the *Px* phase diagrams. Fig. 5 compares the *Px* phase diagrams of Oil NWE in bulk phase with those in confined nanopores. It can be seen from Fig. 5 that the confinement effect shifts the saturation pressure line in the *Px* phase diagrams to lower pressures at lower CO_2 concentrations. However, as CO_2 concentrations increase, the single-phase/two-phase boundary in confined spaces surpasses that of the bulk phase and shifts to a higher-pressure region. Similar to the *PT* phase diagrams, the two-phase region in the *Px* phase diagrams is also reduced in confined nanopores, particularly

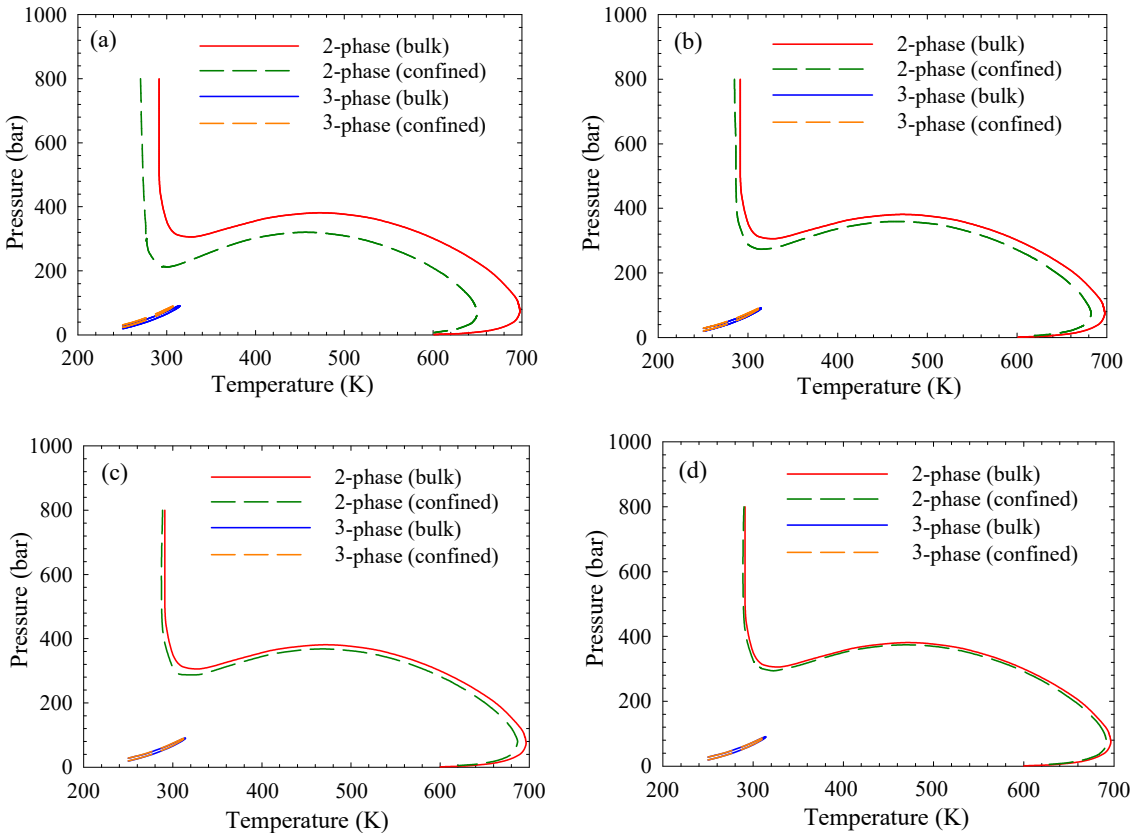

Fig. 6. Comparison between the *PT* phase diagrams of Oil G mixed with 70 mol% CO_2 at bulk and confined nanopores: (a) 10 nm, (b) 30 nm, (c) 50 nm and (d) 100 nm.

at high pressures. Furthermore, the VL_1L_2 three-phase region diminishes in size within the confined nanopores in the *Px* phase diagrams. Unlike the single-phase/two-phase boundary, the VL_1L_2 three-phase region shifts to the upper left side in the *Px* phase diagrams.

3.3 Effect of pore radii on phase diagrams

Pore size plays a fundamental role in determining how confined spaces influence the phase equilibria of reservoir fluids. Fig. 6 shows how pore size affects the *PT* phase diagrams of Oil G, while Fig. 7 depicts the enlarged VL_1L_2 three-phase region in the *PT* phase diagrams. The effect of different pore radii on the *Px* phase diagrams of Oil NWE is presented in Fig. 8. The various pore radii are selected as: 10, 30, 50 and 100 nm. It can be seen from Figs. 6-7 that smaller pore radii lead to a larger shift in both the single-phase/two-phase and the three-phase boundaries in the *PT* phase diagrams. As the pore radii increase, the effect of confinement becomes less pronounced. Additionally, the VL_1L_2 three-phase boundaries shift more significantly at higher pressures and become less distinct in regions of lower pressure. When the pore radius reaches 100 nm, the shifts in both the single-phase/two-phase and the three-phase boundaries in the *PT* phase diagrams become almost negligible.

It can be observed from Fig. 8 that due to the confinement effect, smaller pore sizes lead to a significant shift towards the higher-pressure region of the three-phase boundaries in the *Px* phase diagrams. Additionally, the area of the three-phase region is more substantially suppressed in cases of smaller pore radii. Regarding the single-phase/two-phase boundary, when the pore radius is 10 nm, there is a pronounced shift caused by the confinement effect. It should be noted that in the low-pressure region, the single-phase/two-phase boundary shifts towards the lower-pressure side, while in the high-pressure region, it shifts towards the higher-pressure side. Conversely, for pore radii of 30, 50 and 100 nm, the shift of the single-phase/two-phase boundaries is negligible in the low-pressure region, but it remains noticeable in the high-pressure region. Moreover, the single-phase/two-phase boundaries in these cases shift towards the lower-pressure side in both the lower- and higher-pressure regions.

3.4 Effect of confinement on phase compositions

The impact of confinement on phase fractions was investigated using Oil G as the case study. Fig. 9(a) illustrates the variations in phase mole fractions under isothermal conditions, while Fig. 9(b) illustrates these changes under isobaric conditions. At a given temperature of 280 K within the vapor-liquid two-phase region, the confinement effect results in a higher fraction of the vapor phase and a lower fraction of the liquid phase. In the liquid-liquid two-phase region at the same temperature, confinement leads to a higher fraction of the oil-

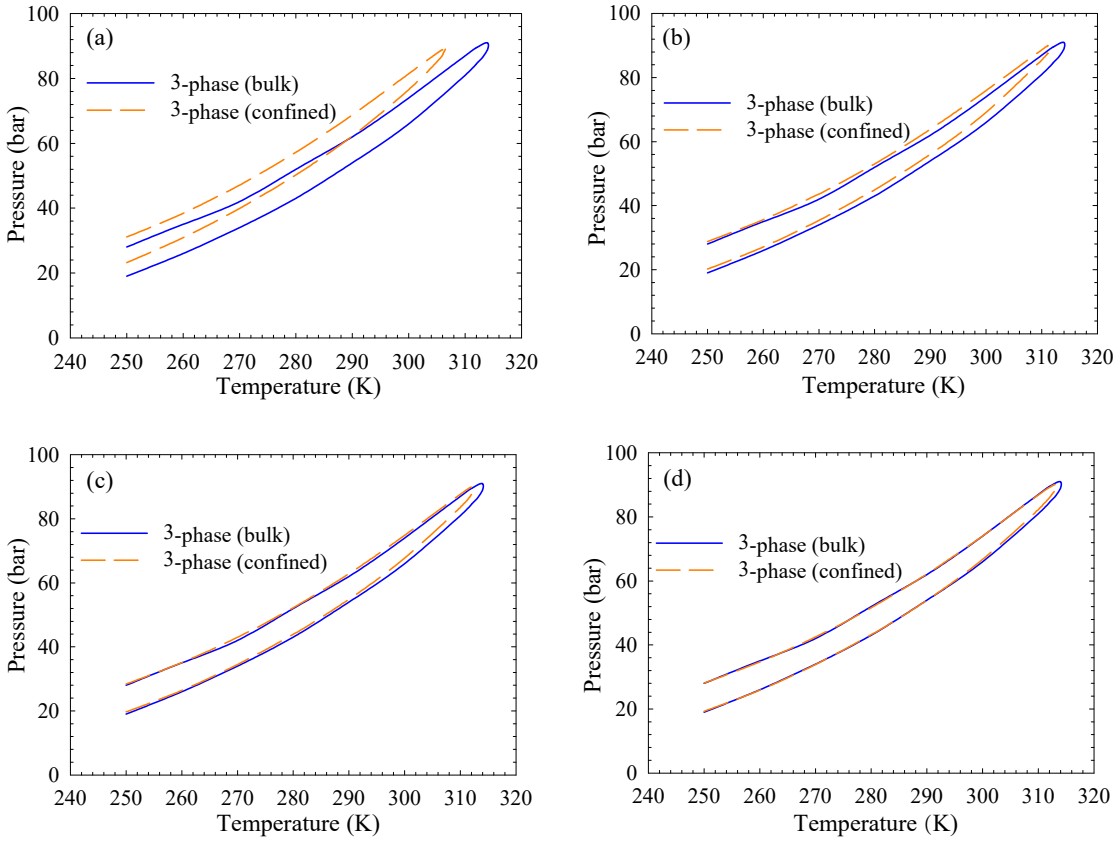

Fig. 7. Comparison between the VL_1L_2 three-phase region in the *PT* phase diagrams of Oil G mixed with 70 mol% CO_2 at bulk and confined nanopores: (a) 10 nm, (b) 30 nm, (c) 50 nm and (d) 100 nm.

rich liquid phase and a lower fraction of the CO_2-rich liquid phase. Within the three-phase region, the confinement effect at 280 K causes an increase in the fractions of both the vapor and oil-rich liquid phases, while the fraction of the CO_2-rich liquid phase decreases.

Under isobaric conditions, at a constant pressure of 40 bar within the vapor-liquid two-phase region, the confinement effect leads to a higher fraction of the liquid phase and a lower fraction of the vapor phase, which contrasts with the behavior observed under isothermal conditions. In the liquid-liquid two-phase region at 40 bar, confinement results in a higher fraction of the CO_2-rich liquid phase and a lower fraction of the oil-rich liquid phase. In the three-phase region, under the same pressure, the confinement effect increases the fraction of the CO_2-rich liquid phase while reducing the fractions of the vapor and oil-rich liquid phases. This analysis highlights how confinement influences phase behavior differently under varying thermal and pressure conditions, demonstrating the complex interplay between the phase fractions and the pressure/temperature conditions.

It is important to note that in actual industry applications, pure CO_2 streams rarely exist, and impurities can shift phase boundaries, modify interfacial tensions, and potentially change the overall phase distribution within confined spaces. These effects would be particularly pronounced near critical points where the system becomes highly sensitive to compositional variations.

4. Conclusions

This work introduces a novel three-phase equilibrium calculation algorithm that accounts for both capillary pressure and critical point shifts in confined spaces. This model can be readily integrated with compositional simulators to simulate CO_2 flooding processes. However, this algorithm is currently applicable only to systems where three hydrocarbon phases exist. For systems containing water or asphaltenes, alternative initial guess strategies for equilibrium ratios or specialized thermodynamic models would be required. Additionally, since the model inherently assumes steady-state phase equilibrium, while fluids in computational grids may not reach instantaneous equilibrium during actual CO_2 flooding scenarios, this introduces inherent limitations when modeling dynamic conditions. The key features of our algorithm are as follows:

1) Capillary pressure and IFTs are determined using the Young-Laplace equation (Young, 1805) and the Weinaug-Katz model (Weinaug and Katz, 1943), respectively. The critical point shift model proposed by Zhang et al. (2018) is used to compute the shift in critical properties of various components.
2) The integration of capillary effects into the three-phase flash algorithm requires the simultaneous updating of

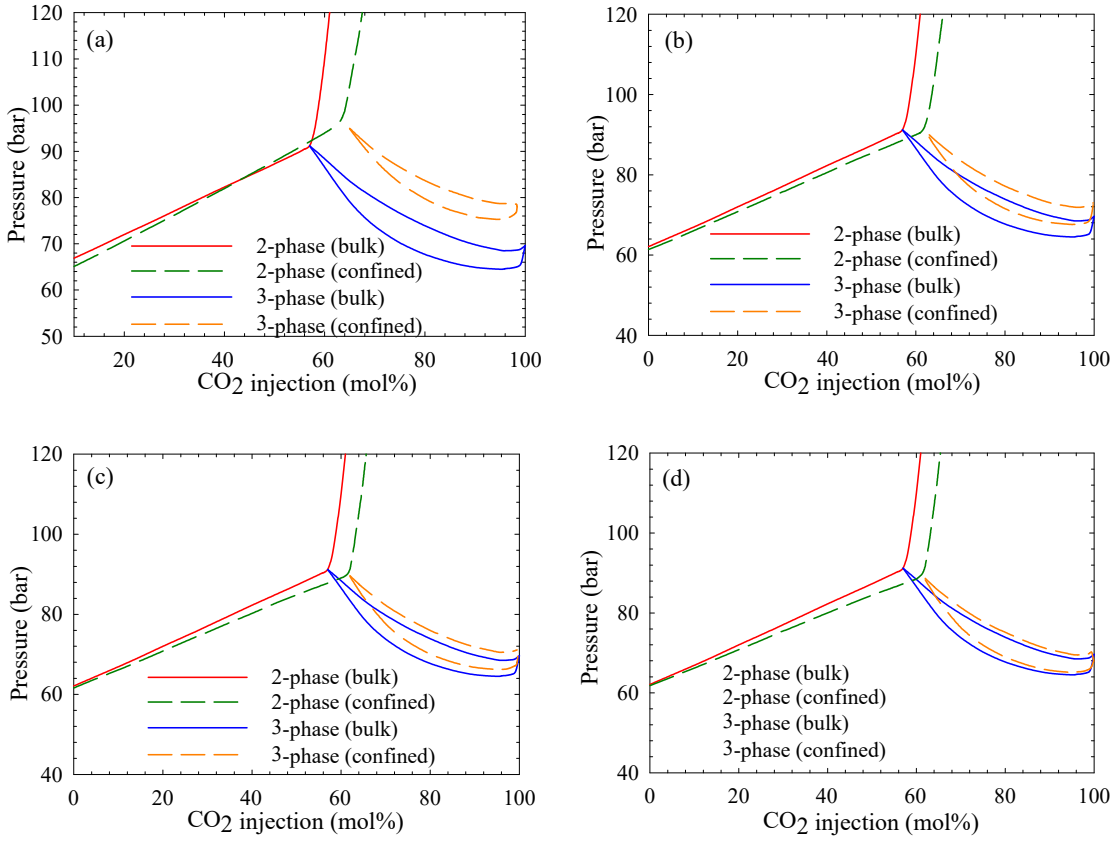

Fig. 8. Comparison between the *Px* phase diagrams of NWE Oil at bulk and confined nanopores: (a) 10 nm, (b) 30 nm, (c) 50 nm and (d) 100 nm.

phase densities, IFTs, capillary pressures, and component fugacities across all phases. When the algorithm converges, it is necessary to ensure that the capillary pressures in the two consecutive iterations are equal.

3) The initialization method and the TR-based approach proposed by Pan et al. (2019) are implemented in the stability test, coupled with the hybrid flash calculation algorithm based on NR and TR methods proposed by Xu et al. (2023) to improve the robustness and efficiency of the newly proposed algorithm.

To validate this methodology, extensive calculations were conducted using three oil samples, each experimentally verified to exhibit VL_1L_2 three-phase behavior during CO_2 injection. The results led to the following conclusions:

1) The calculated single-phase/two-phase and three-phase VL_1L_2 boundaries closely match the experimental data, validating the algorithm's ability to predict the phase behavior of reservoir fluids at low temperatures during CO_2 injection.
2) Confinement alters three-phase VL_1L_2 equilibria, suppressing the two-phase and three-phase regions, shifting the single-phase/two-phase boundary to the lower left and the three-phase region to the upper left in *PT* diagrams.
3) In *Px* diagrams, confinement shifts the single-phase/two-phase boundary to lower pressures at low CO_2 concentrations and higher pressures at high CO_2 concentrations, reducing the two-phase region size and shifting the three-phase region to the upper left.
4) Smaller pore radii cause larger shifts in both single-phase/two-phase and three-phase boundaries. As the pore radii increase, the confinement effect diminishes. In *PT* phase diagrams, the three-phase boundaries shift to a greater extent at higher pressures and become less distinct at lower pressures, with negligible shifts observed at a 100 nm pore radius.
5) In *Px* phase diagrams, the area of the three-phase region is more suppressed with smaller pore radii. For single-phase/two-phase boundaries, a 10 nm pore radius causes pronounced shifts in both low and high-pressure regions, while larger pore radii result in negligible shifts at low pressures but noticeable shifts at high pressures.
6) Under isothermal conditions at 280 K, confinement increases the vapor phase fraction and decreases the liquid phase fraction in the vapor-liquid two-phase region; in the liquid-liquid two-phase region, it raises the oil-rich liquid phase fraction and lowers the CO_2-rich liquid phase fraction; in the three-phase region, confinement increases the vapor and oil-rich liquid phase fractions but decreases the CO_2-rich liquid phase fraction.
7) Under isobaric conditions at 40 bar, confinement leads to a higher liquid phase fraction and a lower vapor phase

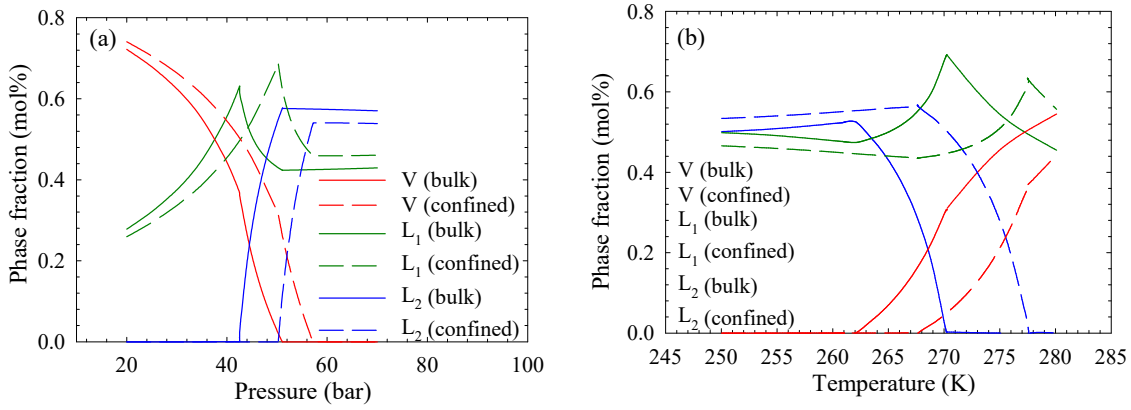

Fig. 9. Comparison between the changes in the phase mole fractions of Oil G with 70 mol% CO_2 injection in the bulk phase and in confined nanopores (10 nm) under (a) isothermal conditions (280 K) and (b) isobaric conditions (40 bar).

fraction in the vapor-liquid two-phase region, opposite to isothermal behavior; in the liquid-liquid two-phase region, it increases the CO_2-rich liquid phase fraction and decreases the oil-rich liquid phase fraction; in the three-phase region, confinement raises the CO_2-rich liquid phase fraction while reducing vapor and oil-rich liquid phase fractions.

Acknowledgements

This study was supported by the project from National Natural Science Foundation of China (No. 52004040).

Conflict of interest

The authors declare no competing interest.

References

Andersen, P. Ø., Brattekås, B., Zhou, Y., et al. Carbon capture utilization and storage (CCUS) in tight gas and oil reservoirs. Journal of Natural Gas Science and Engineering, 2020, 81: 103458.

Bai, B., Elgmati, M., Zhang, H., et al. Rock characterization of Fayetteville shale gas plays. Fuel, 2013, 105: 645-652.

Chen, Z., Shi, J., Zhou, Y., et al. Efficient tracking of vapor-liquid-aqueous-equilibrium/liquid-liquid-aqueous-equilibrium (VLAE/LLAE) phase boundaries. Chemical Engineering Science, 2024, 292: 119984.

Chen, Z., Xu, L., Zhou, Y., et al. A robust and efficient algorithm for vapor-liquid-equilibrium/liquid-liquid-equilibrium (VLE/LLE) phase boundary tracking. Chemical Engineering Science, 2023, 266: 118286.

Chen, Z., Zhou, Y., Li, H. A review of phase behavior mechanisms of CO_2 EOR and storage in subsurface formations. Industrial & Engineering Chemistry Research, 2022, 61(29): 10298-10318.

Conn, A. R., Gould, N. I., Toint, P. L. Trust Region Methods. Englewood Cliffs, New Jersey, USA, SIAM Society for Industrial & Applied Mathematics, 2000.

Firoozabadi, A., Katz, D. L., Soroosh, H., et al. Surface tension of reservoir crude-oil/gas systems recognizing the asphalt in the heavy fraction. SPE Reservoir Engineering, 1988, 3(1): 265-272.

Haugen, K. B., Firoozabadi, A., Sun, L. Efficient and robust three-phase split computations. AIChE Journal, 2011, 57(9): 2555-2565.

Hirschfelder, J. O., Curtiss, C. F., Bird, R. B. The Molecular Theory of Gases and Liquids. New Jersey, USA, John Wiley & Sons, 1964.

Khan, S., Pope, G., Sepehrnoori, K. Fluid characterization of three-phase CO_2/oil mixtures, Paper SPE 24130 Presented at the SPE/DOE Enhanced Oil Recovery Symposium, Tulsa, Oklahoma, 22-24 April, 1992.

Leverett, M. Capillary behavior in porous solids. Transactions of the AIME, 1941, 142(1): 152-169.

Li, H., Yang, D., Li, X. Determination of three-phase boundaries of solvent(s)-CO_2-heavy oil systems under reservoir conditions. Energy & Fuels, 2013, 27(1): 145-153.

Li, Z., Firoozabadi, A. General strategy for stability testing and phase-split calculation in two and three phases. SPE Journal, 2012, 17(4): 1096-1107.

Liu, X., Zhang, D. A review of phase behavior simulation of hydrocarbons in confined space: Implications for shale oil and shale gas. Journal of Natural Gas Science and Engineering, 2019, 68: 102901.

Lu, C., Jin, Z., Li, H., et al. Simple and robust algorithm for multiphase equilibrium computations at temperature and volume specifications. SPE Journal, 2021, 26(4): 2397-2416.

Michelsen, M. L. The isothermal flash problem. Part I. Stability. Fluid Phase Equilibria, 1982a, 9(1): 1-19.

Michelsen, M. L. The isothermal flash problem. Part II. Phase-split calculation. Fluid Phase Equilibria, 1982b, 9(1): 21-40.

Nocedal, J., Wright, S. Springer Series in Operations Research and Financial Engineering. New York, USA, Springer,

2006.

Pan, H., Connolly, M., Tchelepi, H. Multiphase equilibrium calculation framework for compositional simulation of CO_2 injection in low-temperature reservoirs. Industrial & Engineering Chemistry Research, 2019, 58(5): 2052-2070.

Peng, D. Y., Robinson, D. B. A new two-constant equation of state. Industrial & Engineering Chemistry Fundamentals, 1976, 15(1): 59-64.

Petitfrere, M., Nichita, D. V. Robust and efficient trust-region based stability analysis and multiphase flash calculations. Fluid Phase Equilibria, 2014, 362: 51-68.

Petitfrere, M., Nichita, D. V. On a choice of independent variables in Newton iterations for multiphase flash calculations. Fluid Phase Equilibria, 2016, 427: 147-151.

Rachford Jr, H. H., Rice, J. Procedure for use of electronic digital computers in calculating flash vaporization hydrocarbon equilibrium. Journal of Petroleum Technology, 1952, 4(10): 19-13.

Robinson, D. B., Peng, D. Y., Chung, S. Y. The development of the Peng-Robinson equation and its application to phase equilibrium in a system containing methanol. Fluid Phase Equilibria, 1985, 24(1-2): 25-41.

Sherafati, M., Jessen, K. Stability analysis for multicomponent mixtures including capillary pressure. Fluid Phase Equilibria, 2017, 433: 56-66.

Song, Z., Li, Y., Song, Y., et al. A critical review of CO_2 enhanced oil recovery in tight oil reservoirs of North America and China. Paper SPE 196548 Presented at the SPE/IATMI Asia Pacific Oil & Gas Conference and Exhibition, Bali, Indonesia, 29-31 October, 2019.

Sun, H., Li, H. Minimum miscibility pressure determination in confined nanopores considering pore size distribution of tight/shale formations. Fuel, 2021, 286: 119450.

Weinaug, C. F., Katz, D. L. Surface tensions of methane-propane mixtures. Industrial & Engineering Chemistry, 1943, 35(2): 239-246.

Wilson, G. M. A modified Redlich-Kwong equation of state, application to general physical data calculations. Paper 15C Presented at 65th National AIChE Meeting, Cleveland, Ohio, 15 May, 1969.

Xu, L., Li, S., Li, H. Hybrid multiphase flash calculation algorithm based on simultaneous solution of equilibrium ratios and phase fractions. Industrial & Engineering Chemistry Research, 2023, 62(22): 8981-8992.

Yang, G., Fan, Z., Li, X. Determination of confined fluid phase behavior using extended Peng-Robinson equation of state. Chemical Engineering Journal, 2019, 378: 122032.

Young, T. III. An essay on the cohesion of fluids. Philosophical Transactions of the Royal Society of London, 1805, 95: 65-87.

Zhang, K., Jia, N., Li, S., et al. Thermodynamic phase behaviour and miscibility of confined fluids in nanopores. Chemical Engineering Journal, 2018, 351: 1115-1128.